Investigating Rayleigh wave anisotropy in faulted media with three-component beamforming
Insights from numerical models and applications for geothermal exploration

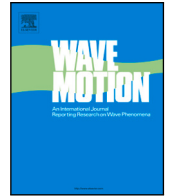Kennedy, Heather; Finger, Claudia; Löer, Katrin; Gilligan, Amy

Important note
To cite this publication, please use the final published version (if applicable).
Please check the document version above.

Investigating Rayleigh wave anisotropy in faulted media with three-component beamforming: Insights from numerical models and applications for geothermal exploration

Heather Kennedy [a],*, Claudia Finger [b], Katrin Löer [c], Amy Gilligan [a]

[a] *University of Aberdeen, School of Geosciences, Aberdeen, AB24 3UE, Aberdeenshire, United Kingdom*
[b] *Fraunhofer IEG, Fraunhofer Institution for Energy Infrastructures and Geothermal Systems IEG, Bochum, Germany*
[c] *Delft University of Technology, Delft University of Technology, Delft, Netherlands*

ARTICLE INFO

ABSTRACT

Rayleigh waves are prevalent in the ambient seismic noise wavefield and are thus often exploited in passive seismic methods to characterise the near subsurface. In fractured or faulted media, Rayleigh waves show anisotropic velocities that could provide information on the fault properties. However, the exact relationship between Rayleigh wave anisotropy and true anisotropic structures is not well known. This study used a three-component (3C) beamforming toolbox to analyse numerical full waveform seismic wave propagation from conceptual models of fractured media, which depict the nonlinear physical behaviour of the wave. We identify Rayleigh waves in the synthetic data produced from a single point source at different locations, compare observed Rayleigh wave anisotropy to structural anisotropy, and assess the effect array design and source distance have on Rayleigh wave analysis and observed anisotropy. Numerical analysis shows that the smaller the velocity contrast between fault and surrounding rock, the more complex the anisotropic response. We find that the slow directions of Rayleigh wave propagation can be a better indicator of fault strike than the fastest direction, when the velocity contrast between the two media is small.

1. Introduction

Rayleigh waves are elastic waves propagating along the surface of a medium with a frequency-dependent depth sensitivity causing dispersive behaviour [1]. In seismology, Rayleigh waves are observed in the high amplitude surface wave train excited by earthquakes or active sources in seismic surveys, and they often constitute the dominant component of the ambient seismic noise wavefield excited, for example, by oceanic microseisms [2].

Array-based techniques, such as beamforming, have been used to analyse ambient seismic noise data and assess wavefield properties such as polarisation, velocity, and direction of propagation, allowing us to discriminate Rayleigh from other waves in ambient noise and to link their properties to medium properties [3,4]. While shear-velocity profiles are routinely derived from Rayleigh wave dispersion curves, showing velocity variation with frequency [5], beamforming also gives access to velocity variation as a function of azimuth [4], which in the following we refer to as azimuthal Rayleigh wave velocity anisotropy, or short anisotropy. Observed anisotropy, which is usually a mix of intrinsic and extrinsic anisotropy [6], is a feature of the medium, and when seismic

---

waves travel through an anisotropic medium they also show anisotropic features, such as velocity variations with direction or polarisation (as in shear wave splitting), depending on spatial scale and seismic wavelength [6].

Previous studies [7–10] have shown a relation between anisotropy at depth and fractures. Fractures and faults provide an invaluable source of secondary permeability for circulation of hydrothermal flow in geothermal fields [11]. Hence, their characterisation can provide crucial insight into the potential of a geothermal system and help advance the energy transition. Kennedy et al. [7] used three-component (3C) beamforming of ambient seismic noise to look at Rayleigh wave anisotropy, as a function of frequency, and related the fast directions of Rayleigh waves to fault variations at depth. This was based on the hypothesis that Rayleigh waves would travel faster parallel to the fault rather than perpendicular to the fault due to changes in the elastic constants of the structures in the surrounding lithology compared to the fault itself [12–14]. The fastest observed velocities correspond to specific azimuths, thus providing an indication of the strike of a fault at different depths.

Luo and Yao [8] derive a three-dimensional (3D) high-resolution upper crustal azimuthally anisotropic model of shear wave velocity using surface wave (specifically Rayleigh wave) dispersion data from ambient seismic noise. They found that fast directions of azimuthal anisotropy were consistent with local geological units, seeing variations at different depths. Li and Peng [9] use shear wave splitting (SWS), a method that analyses the splitting of horizontally and vertically polarised shear waves (shear horizontal (SH) and shear vertical (SV), respectively) in anisotropic media [15], to look at fast directions related to regional compressional stress and local fault strikes. They found that some near-fault stations display fast directions parallel to the fault strikes [9]. Boness and Zoback [10] measured SWS using microearthquakes to distinguish between stress induced anisotropy or structural anisotropy, they found that fast directions were parallel to the strike of structural anisotropy (such as faults) and that the fast directions were perpendicular to stress-induced anisotropy (such as microcracks) [10].

The interaction of Rayleigh waves with faults and similar structure can result in nonlinear behaviour which has been observed in other fields of wave propagation and described mathematically, for example, by [16–18].

This study addresses the following research questions: First, if the fast direction corresponds to the orientation of a fault, and what effect different geological settings have on Rayleigh wave anisotropy observed with 3C beamforming. Second, if all arrays retrieve this fast direction equally well, answering the question: What is the ideal array design that does not bias the observed anisotropy?

We test the relation of fault strike and fast directions in Rayleigh wave anisotropy using three-component (3C) beamforming of synthetic data created by numerical wavefield modelling. 3C beamforming (first formulated by [19–22]) is an array-based technique for wavefield analysis which enables the determination of propagation directions and propagation velocities, and, thus, allows for the inference of surface wave anisotropy. While beamforming has become a popular method for ambient noise analysis, this study examines transient Rayleigh waves generated by a single source. This idealised scenario should allow us to focus on the effect of the structure as well as the array geometry on (perceived) wave velocity and direction and mitigate the effect of multiple simultaneous sources [23].

The 3C beamforming method used in this study extracts the polarisation, phase velocities, and azimuths of different wave types in the seismic wavefield as a function of frequency [24]. Here, we focus on azimuthal anisotropy observed as variations in surface wave velocity as a function of propagation direction. An anisotropy curve is fitted to the azimuth-velocity estimates obtained from beamforming (as in [4,25]) and by assessing the slow and fast directions of these curves, we should be able to infer the strike of the faults within a medium. In this study, we scrutinise this hypothesis using synthetic data from numerical models.

In the next section we introduce the numerical modelling scheme, the geological scenarios considered, and the beamforming method. This is followed by a presentation of the beamforming results of the synthetic datasets considering different models as well as different receiver and source layouts. We conclude with a discussion and a summary of our main findings, highlighting the improved understanding of Rayleigh wave behaviour in fractured media, fast directions in relation to fractures, understanding the importance of modelling parameters and applications for geothermal field characterisation.

2. Methods

The goal of the numerical experiment was to build a conceptual model of a fault system in a 3D homogeneous half-space, which is illuminated by a single point source generating a transient wavefield that propagates across the fault and is recorded by an array of receivers. The wavefield is then analysed with a 3C beamformer, which identifies the Rayleigh wave arrival and determines its velocity and direction of propagation. Repeating the simulation for varying source positions allows us to measure Rayleigh wave velocity as a function of azimuth, i.e., azimuthal surface wave anisotropy.

By changing the elastic parameters of the model we then investigate the effect of structural changes on the measured anisotropy. Further, varying array designs are tested to get insight into the influence of the array geometry on measured velocities and directions.

We highlight again that we do not model an ambient noise wavefield but transient waves from individual sources. While this makes our experiment less comparable to ambient noise applications, it allows us to investigate the effect of structure and array design on observed anisotropy separately from the effects of a complex wavefield generated by multiple sources.
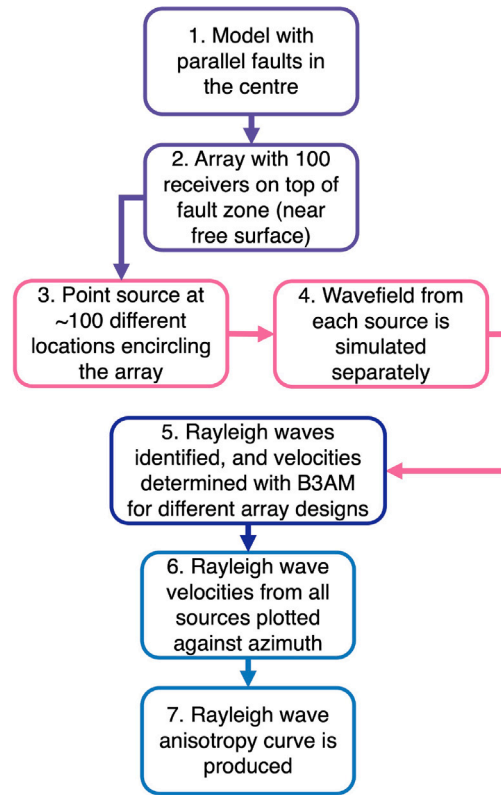
Fig. 1. Workflow of methodology, this workflow was applied to both conceptual models of fractured media (with and without faults).

2.1. Rotated staggered grid - finite difference scheme

The first step of our workflow (Fig. 1) comprises numerical wavefield modelling. In this study, a Rotated Staggered Grid (RSG) - Finite Difference (FD) scheme [26] is used to simulate the full elastic 3D wavefield through the different models. The RSG-FD was used for its excellent capability at handling heterogeneous models with stark contrasts, for instance, when fractures are implemented. Furthermore, the RSG FD has been proven accurate when modelling Rayleigh waves [27]. Anisotropy was introduced through changes in elastic properties according to the fault geometries and properties.

A conceptual model with a homogeneous half-space was used for each medium in the simulations. Each model has a free surface at the top of the model with the parameters of a vacuum (as this is how the RSG-FD implements a free surface) where surface waves are created. Absorbing boundary conditions were applied to the sides and bottom of the model. A grid size of 150 x 300 x 300 grid points was used, equal to 1.5 x 3 x 3 km (depth x N-S x E-W), with a grid spacing of 10 m. Anisotropy was applied as five faults, 40 m in width (including "damage zone", 10 m on each side, around each one) and the full length of the model (no variation with depth), and 100 m apart, as fractures tend to be in multiples and parallel to each other based on stress orientations. Velocities and densities used to implement these conditions are shown in Table 1. For the conceptual models, values from two different examples of fractured media were used. These case studies were two geothermal field locations (Section 2.2) and values for both the surrounding rock and fault-"fill" were decided based on literature for the two areas and known parameters of rocks [28–33].

The seismic source was implemented as a single point source located at 0.4 km depth and moved counter-clockwise around the array in 5°-steps, starting at $270° = South$. A Ricker wavelet [34] of central frequency $f_c = 3\ Hz$ was used. Producing an isolated Rayleigh wave in a 3D model requires a large distance between source and receiver(s) for body and surface waves to separate, resulting in a large model and, hence, high computational costs. Instead, the distance between the source and receiver array was chosen to be large enough for the wavefront to arrive at the receivers as a plane wave as required when applying beamforming. 1.5 km was determined empirically to be a sufficient distance between source and receiver array for the considered wavelengths. P- and Rayleigh waves are then distinguished via polarisation analysis during beamforming.

The individual simulations from multiple, subsequent source locations generated a Rayleigh wave from each corresponding source azimuth enabling anisotropy analysis. Full 360° illumination was used to capture the effect of asymmetrical arrays in which the source-receiver spacing varies as a function of azimuth and as a result the Rayleigh wave arrival time window can vary as well.

Rayleigh wave velocities (estimated as $V_R = 0.9 \times V_S$ [35]) are between 567 ms^{-1} and 2700 ms^{-1}, and the expected wavelengths ($\lambda = v/f$) are in the range of 189 m to 900 m. The fault width-to-wavelength ratio will affect the behaviour of Rayleigh waves when

Table 1

Parameters for the two geological scenarios used within the conceptual models, showing the compressional velocity (V_p), shear velocity (V_s), V_p/V_s ratio of 1.6 to 1.77 and density (ρ) of both the surrounding rock, the "fill" of the fault and the damage zone of the fault. V_p and V_s in ms^{-1}, and ρ in kgm^{-3}.

Geological scenarios	Surrounding rock			Fault "fill"			Damage zone		
	V_p	V_s	ρ	V_p	V_s	ρ	V_p	V_s	ρ
Los Humeros, Mexico	4500	2700	2565	2400	1357	2039	2600	1472	2100
Cornwall, UK	4800	3000	2640	1100	630	1760	1300	745	1660
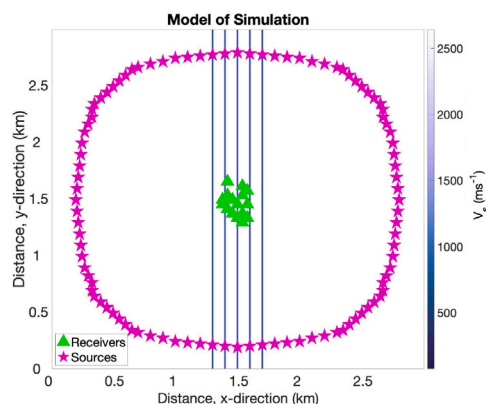
Fig. 2. Source and receivers layout, with five parallel faults ($\theta = 0°$), 40 m width each and 100 m apart, with individual point sources at all azimuths for each simulated wavefield shown together for reference of the location of the sources, for a conceptual model of Los Humeros. The individual points sources were arranged such that if shown together, they would provide a circular source layout, therefore allowing the sources to interact with the faults at different angles.

encountering a fault. The preferred ratio used was 1:10, which is based on the real-life fault width-to-wavelength ratio in the Los Humeros study area. Although slightly higher frequencies are used for the conceptual models than real-world examples, the ratios are kept the same (see Fig. 2).

Runtimes are, on average, approximately 1 h and 18 min per simulation (± 20 *minutes*), with 3 nodes and 23 tasks per node for each simulation on a high-performance computing (HPC) cluster.

2.2. Case studies for numerical models

Conceptual models based on geological parameters from two geothermal sites were used to assess Rayleigh wave behaviour in a fractured medium: Los Humeros Geothermal Field (LHGF) in Mexico, and undergoing geothermal reservoir developments in Cornwall in England, UK, mainly based at the geothermal reservoir at Eden Geothermal site [36].

The LHGF in Mexico is situated in the Los Humeros Volcanic Complex in the eastern part of the Trans-Mexican Volcanic Belt [37] and was the area of focus in a previous study [7]. It has been used for geothermal exploration for many decades [38] and is in an extremely complicated geological area with an active tectonic fault system [39]. There are two main calderas and resurgence faults, which are the main source of secondary permeability for the transportation of hydrothermal fluid flow through the reservoir to be then pumped up to the surface for electricity production [39]. Seismic anisotropy investigation was conducted to understand how deeply these faults permeated into the subsurface [7]. One main rock type observed within the region is andesitic lavas, formed from a variety of explosive and effusive eruptions throughout the region's history, whilst the resurgence faults are found to have quartzite/sandstone deposits due to retrograde mineralisation caused by hydrothermal alteration [28,40]. The andesitic rock with quartzite faults is the main focus of this study, which is to recreate a simplified LHGF in a numerical simulation to compare synthetic anisotropy results to previously acquired anisotropy, providing a fuller understanding of how Rayleigh wave velocities interact with the faults in this geothermal field.

Cornwall is situated in the southwest of the UK. It is dominated by a large granite intrusion and, due to its radiogenic granite outcrops, has the highest geothermal heat flow in the UK [41]. Several studies have shown the heat flow using borehole data, showing temperatures of 200°C at 5 km depth [42]. Geophysical studies have been conducted on the extent of the granite, including gravity surveys that show negative Bouguer anomalies associated with granite [41]. They suggest that the exposed granites are cupolas (an upward protrusion from the roof of a large igneous intrusion [43]) on a single elongated batholith, called the Cornubian batholith, which reaches a depth of at least 8 km, potentially 20 km [41]. The St Austell granite, a large granite pluton protruding from the Cornubian Batholith, is surrounded by metasediments and metamorphosed country rock due to the intrusion event of the granite [44]. The granite, specifically the St Austell pluton, has faults/fractures throughout, which tend to be filled with clay [31,45,46]. This extensively clay-filled fractured granite is numerically modelled to assess the differences in Rayleigh wave anisotropy for a geologically differing geothermal reservoir. As St Austell granite in Cornwall, is a fractured medium different from Los Humeros, parameters based on geology were used in a conceptual model to look at how drastically different parameters can affect Rayleigh wave propagation (Table 1).

Retrograde Rayleigh Wave
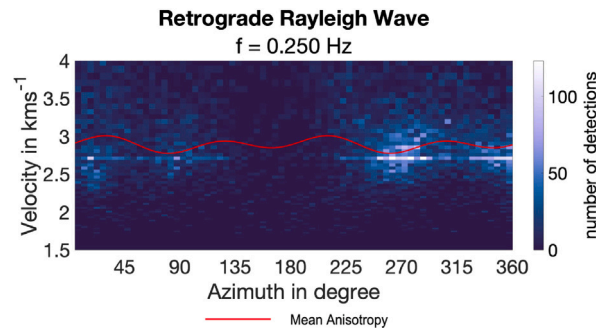
Fig. 3. Histogram for velocity-azimuth pairs and the maximum response for each time window together, showing the change in velocity as a function of azimuth for all time windows in the form of the anisotropy curve of a Retrograde Rayleigh wave of a frequency of 0.25 *Hz*. A number of detections from the ambient noise wavefield (colour bar) and the mean anisotropy curve, calculated from the anisotropy of multiple bootstrap resamples (red line). Based on Fig. 6 from Kennedy et al. [7].

2.3. Beamforming

Single-component (1C), vertical, beamforming is a commonly employed array processing technique for estimating the azimuth and slowness of the seismic waves arriving at an array [47,48]. It uses the differential travel times of the plane wavefront due to a specific slowness and back azimuth [3]. If the single-station recordings are appropriately shifted in time for a certain back azimuth and slowness, all signals with the matching back azimuth and slowness will sum constructively [3].

Three-component (3C) beamforming, similar to 1C beamforming, can extract the azimuths and phase velocities of coherent waves in a finite time window [25]. Additionally, it can decompose polarisation of the wave from the energy distribution among the vertical and horizontal components of the sensors, enabling the differentiation of the different wave types such as Rayleigh and Love waves [4,25].

Beamforming is often used for ambient noise wavefields [4,48,49], although it was originally used for earthquake analysis [3]. This is because ambient noise provides a large degree of source coverage from several locations, which creates significant surface wave energy that is widely available even when seismicity is typically low [4]. A general assumption is that waves arriving at the array are planar. Thus, the analysis of seismicity close to the receiver network require different methods, such as matched field processing (MFP) [50]. B3AM, a beamforming toolbox for 3-component ambient noise [24], is the 3C beamforming method used in this study.

This study focuses on the analysis of retrograde Rayleigh waves, which typically constitute the fundamental mode and are often the dominant component in the ambient noise wavefield [4,25]. Rayleigh waves are described as an ellipse in the vertical-radial plane [4]. There are two different types of Rayleigh waves, prograde and retrograde, with different particle motions: prograde Rayleigh wave's elliptical motion is parallel relative to the direction of propagation [51], whilst retrograde Rayleigh waves are anti-parallel [52].

Beamforming is applied to one-time window at a time. When applied to ambient noise, the window length is typically determined by the largest period in the signal [4,25]. For the synthetic data in this study, comprising a transient wavefield, the time windows need to be adjusted so that one Rayleigh wave will arrive within one-time window, based on the time it takes for the waves to traverse the maximum aperture of the array. Time windows overlapped each other by 75% and a cosine tapering function was applied to prevent artefacts in the Fourier transformation.

2.4. Anisotropy analysis

Anisotropic velocities in low-frequency Rayleigh waves could indicate faults continuing at depth within a fractured medium. Fig. 3 shows the variation in velocity of passive seismic data from the Los Humeros Geothermal Field in Mexico. The surface waves identified in the ambient noise wavefield were analysed at discrete frequencies and in short time windows. A maximum response for each time window of the data was chosen, and all the velocity-azimuth pairs were plotted into the histogram (Fig. 3). The anisotropy curve was fitted to the data to describe the velocity and azimuth variation [25]. We will not use such a histogram for the synthetic experiment instead, for each point source, the Rayleigh wave velocity (as measured by the beamformer) will be plotted against azimuth to give an anisotropy relationship.

In Kennedy et al. [7], anisotropy parameters (for Fig. 3 were $a_0 = 2.8924$, $a_1 = 0.0476$, $a_2 = 0.0167$, $a_3 = -0.0522$ and $a_4 = 0.0594$) are retrieved by fitting the anisotropy equation (1)

$$v(\theta) = a_0 + a_1 cos(2\theta) + a_2 sin(2\theta) + a_3 cos(4\theta) + a_4 sin(4\theta), \tag{1}$$

[53] to the velocity versus azimuth histograms for both Love and Rayleigh waves using a nonlinear programming solver that searches for a local minimum of a fit (MATLAB function called fminsearch, for more details refer to MathWorks [54,55]). Here, θ is the direction of propagation, measured anti-clockwise from the east, v is the phase velocity in kilometres per second (km^{-1}), and a_i
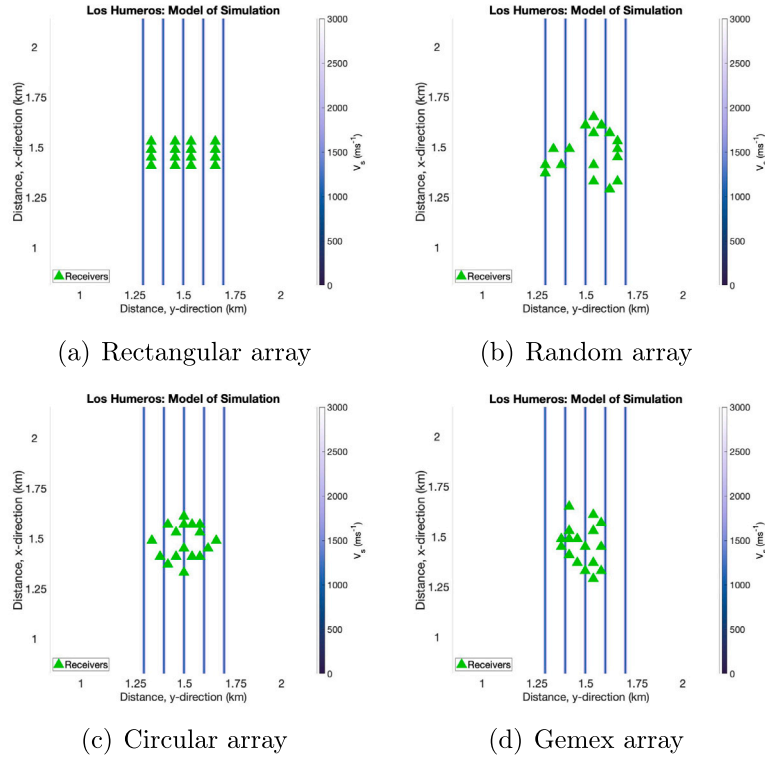
Fig. 4. Array designs with five parallel 40 m faults for the conceptual model of Los Humeros, using 17 receivers (16 for (a)), for (a) Rectangular array d_{max} = 342 m, (b) Random array d_{max} = 394 m, (c) Circular array d_{max} = 320 m and (d) Gemex array d_{max} = 379 m. Theoretical array responses can be seen in the supplementary materials (Fig. A.15).

are the anisotropy parameters. From the anisotropy curve we obtain the azimuth of the fast direction (here 35 and 210°). Fast directions of anisotropy have been linked to fault strikes when looking at anisotropic models [8], which denotes this important relation between fast direction and structural anisotropy. We will investigate in detail in this study how this is related to the strike of the fault.

In the case of synthetic data, the velocity for each identified retrograde Rayleigh wave was calculated using the corresponding wavenumber, k (picked at the point of the maximum beam energy response (red cross point)), and f_c = 3 Hz (we looked at beam power results for f = 3 Hz which is the central frequency of the model) using $v = f_c/k$. These velocities were then visualised in azimuth vs velocity plots for all array designs (Fig. 9), for both conceptual models. The anisotropy curves seen (Fig. 9) are fitted to the azimuth vs velocity data in the same way as Fig. 3, using a fitting function of (a, θ) of Eq. (1) with a nonlinear programming solver that searches for the local minimum.

2.5. Array design

The velocities and azimuths detected with B3AM can be influenced by array effects [56] The observed anisotropy can therefore be biased by so-called apparent anisotropy, which results from an anisotropic distribution of stations, for example [7,57].

To account for the apparent anisotropy, homogeneous models, with no anisotropy applied, were simulated through numerical modelling. This enabled the analysis solely of the array's effect on the synthetic data.

An ongoing debate in the ambient noise community is the best array design for the optimum ambient noise studies [56,58,59]. Tests have been done in the past [56,60,61] to check this as well as accounting for array effects on azimuth. Studies suggest that the best array designs are those without a preferential direction, for example, triangular, circular, or random arrays [56,58]. Varying the number of receivers changes the wavenumber range the array is sensitive to in the beamformer analysis. In this study, four main receiver layouts were tested (Fig. 4): rectangular, random, circular and GEMex (the seismic array deployed in Los Humeros, Mexico, for the GEMex project, used in [7,49]). A 100-receiver array was implemented to collect synthetic data, which enabled specific receivers to be selected afterwards and to realise different array layouts and receiver spacings; receiver locations were restricted by the 100-station array. This means that a simulation for a chosen model would only need to be run once rather than repeatedly for the different array designs.

(a) Times series of Z component   (b) Times series of Y component
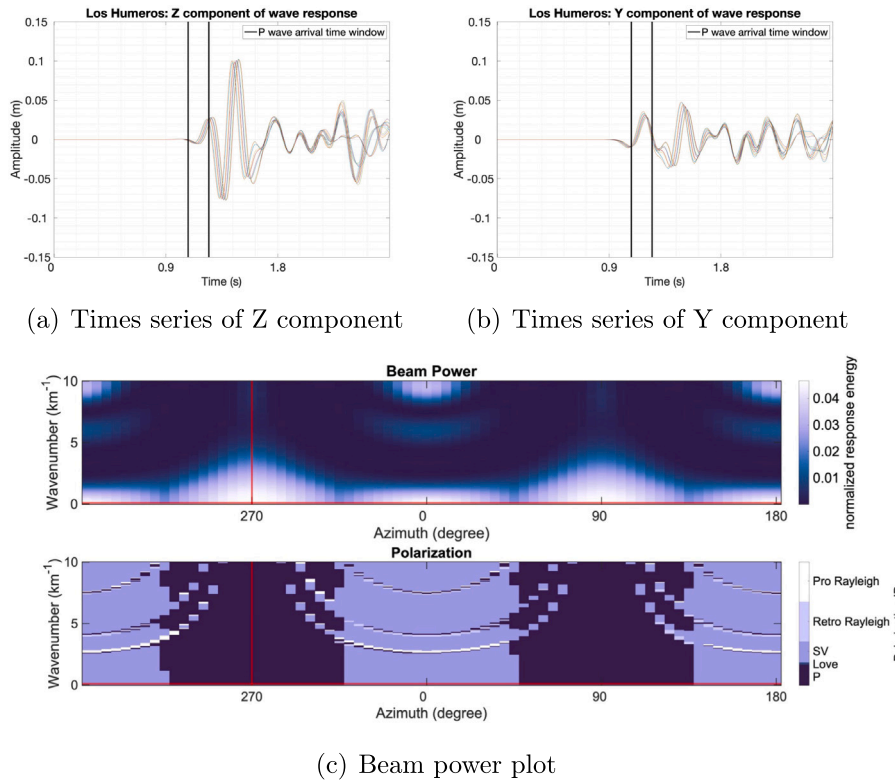
(c) Beam power plot

Fig. 5. Seismic traces and beam power plot for (a) times series in *z*-direction (depth) with P wave arrival highlighted, (b) times series in *y*-direction (N-S) with P wave arrival highlighted (c) Beam power plot depicting the P arriving from the 270° = South, shown by the red cross with a velocity of 8571 ms⁻¹ (time window = 6, $t = 0.71$ to 0.83 s). This is for a rectangular array with 16 receivers for the conceptual model of Los Humeros with faults.

One key component in array design is the receiver spacing, the two most important values being the minimum, d_{min} and maximum d_{max} receiver spacing. The overall rules for the array spacing are based on recommendations by Tokimatsu et al. [62], relating minimum and maximum receiver spacing, d_{min} and d_{max}, to the smallest and largest resolvable wavelength, λ_{min} and λ_{max}: [49].

$$\lambda_{max} < 3d_{max} \tag{2}$$

$$\lambda_{min} > 2d_{min} \tag{3}$$

However, since receiver spacing is not necessarily identical for all azimuths, more accurate estimates of λ_{min} and λ_{max} are typically obtained by considering the wavenumber limits in the array response function, ARF [63]. All arrays had $d_{min} = 40$ m, whilst d_{max} varied between 320 and 394 m (all apertures are within conditions recommended in Eqs. (2) and (3)). We used 17 receivers in each array (16 in the case of the rectangular array) to allow for the direct comparison to real data results from [7], where a maximum of 17 receivers was used.

3. Results

3.1. P and Rayleigh wave arrivals

The maximum value in this plot (Fig. 5) corresponds to the wavenumber-azimuth pair that fits the observed wavefield best in this time window (shown by red cross); the wave type (depicted by the Polarisation ID, which indicates the different wave types due to their respective polarisation [25]) in the bottom plot corresponding to this point is the dominant wave type arriving at this time window. In Fig. 5(c), this is the P wave. Comparably, in Fig. 6 in a later time window, we see evidence of the retrograde Rayleigh wave, shown by the high amplitude for the vertical component (6(a)), smaller amplitude in the horizontal (6(b)) and dominant wave type shown as Retrograde Rayleigh arriving from the correct source direction of 270° = *South* (6(c)). Thus, the particle motion of the Rayleigh wave describes a vertically polarised ellipse, as we would expect for a mostly homogeneous medium without a sharp velocity contrast at depth and a Poisson ratio close to 0.25 [64].

The P wave and retrograde Rayleigh wave, in Figs. 5 and 6 are arriving from 270° = *South* due to the source position in these examples. The P wave has a high velocity of 8571 ms⁻¹ travelling a lot faster than the Rayleigh wave with a velocity of 1985 ms⁻¹,

(a) Times series of Z component   (b) Times series of Y component
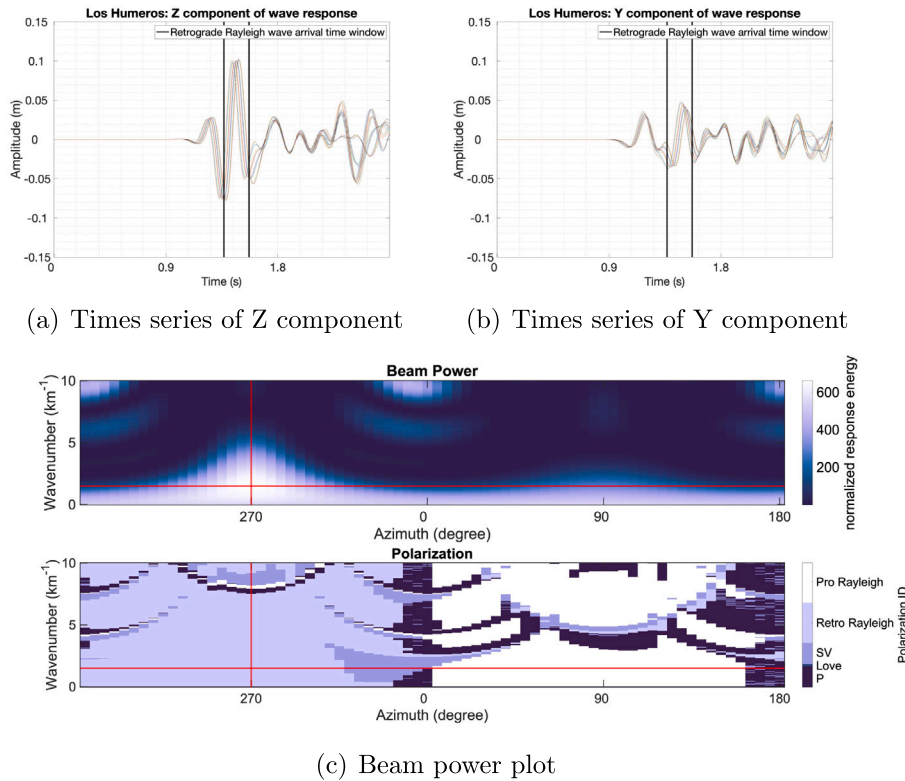
(c) Beam power plot

Fig. 6. Seismic traces and beam power plot for (a) times series in z-direction (depth) with retrograde Rayleigh wave depicted, (b) times series in y-direction (N-S) with retrograde Rayleigh wave arrival depicted $t = 1.54$ to 1.65 s, (c) Beam power plot depicting the retrograde Rayleigh wave arriving from the $270° = South$, shown by the red cross with a velocity of 1985 ms^{-1} (time window $= 13$, $t = 1.54$ to 1.65 s). This is for a rectangular array with 16 receivers for the conceptual model of Los Humeros with faults.
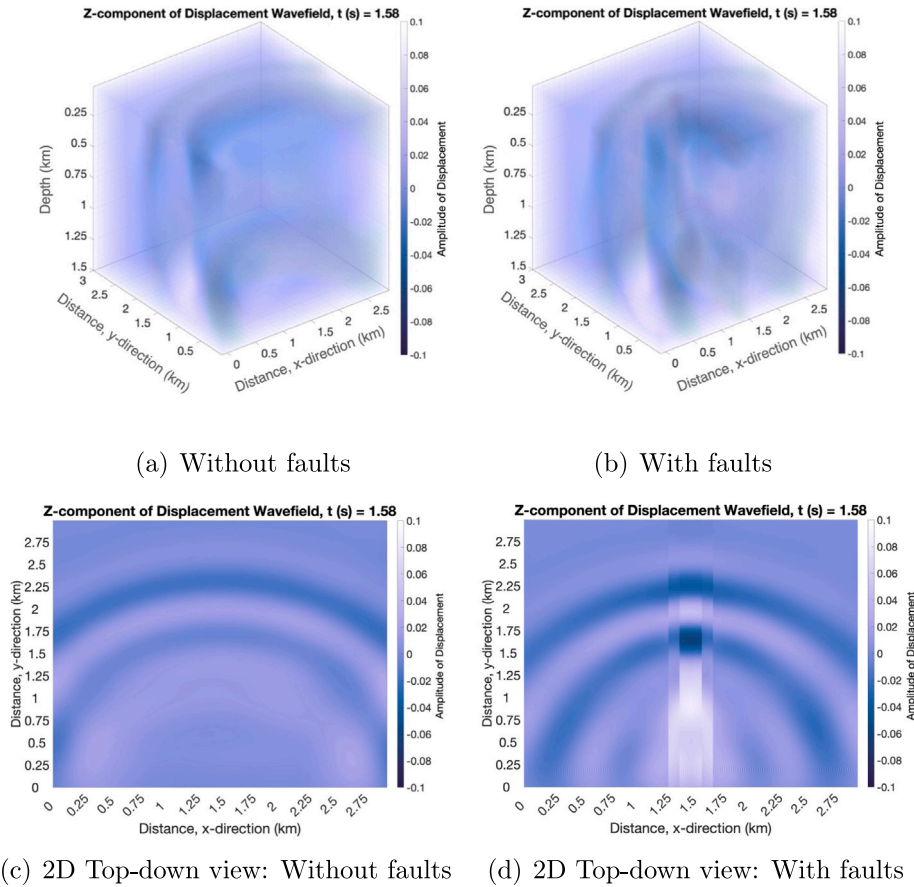
which is to be expected. As the source is moved, it will interact with the fault and arrive at the array at different angles, altering the velocity and azimuth of the identifiable Rayleigh wave and enabling anisotropy analysis.

Fig. 7 shows examples of three-dimensional (3D) and two-dimensional (2D) snapshots for the conceptual model using parameters from Cornwall, at $t = 1.58$ s (within the time window where Rayleigh waves are depicted to arrive) of the synthetic waves propagating outwards from the source location ($270° = South$) through the model. Fig. 7(a) and (c) represent a model without faults, whilst Fig. 7(b) and (d) represent a model with faults. The wave is propagating through the model, both with and without a fault present, with time and has a clear nonlinear relationship in the wave's elastic behaviour, particularly when the wave is interacting with the fault [16–18,65–67]. This (3+1) dimensional distribution has been described in terms of nonlinear physics [16–18,65] in relation to differential time-dependent functions by [16–18], they observe Korteweg–de Vries type equations to describe this behaviour [16,17]; as well as 2D examples referring to auto-Bäcklund transformations to describe displacement and velocity of different waves [18,66,67]; thus providing some mathematical insight into our observations.

3.2. Rayleigh wave identification

B3AM was used on every synthetic dataset to identify a retrograde Rayleigh wave for velocity analysis. Similar to Fig. 6(c), beam power plots were produced for all array types to assess whether retrograde Rayleigh waves could be identified in the wavefield. For a retrograde Rayleigh wave to be positively identified, it must be present within a time window after the arrival of the P wave and be from the same direction as the source location so that it is clear that the Rayleigh wave is from a direct wave. All beam power plots for the different arrays (rectangular, random, circular and GEMex) showed an identifiable retrograde Rayleigh wave, mostly in time window $= 13$, $t = 1.54$ to 1.65 s (examples can be seen in Fig. A.16 in Appendix A). All beam power plot examples are for the conceptual model of Los Humeros. Similar analyses were also conducted on conceptual models of Cornwall so that the differences in Rayleigh wave anisotropy depending on geologically different fractured media could be assessed.

We estimate Rayleigh wave velocity as a function of azimuth by placing sources in different directions with respect to the array and the faults. Fig. 8 shows beampower plots from correctly identified Rayleigh waves from different directions. In Fig. 8(a), we see a clear retrograde Rayleigh wave coming from the South, which correlates correctly to the source location. Fig. 8b is also a direct retrograde Rayleigh wave, in this case coming from the East ($0° = East$), which matches the source direction used for this simulation.

(a) Without faults

(b) With faults

(c) 2D Top-down view: Without faults   (d) 2D Top-down view: With faults

Fig. 7. 3D and 2D snapshots at $t = 1.58$ s of retrograde Rayleigh wave propagating through a model for a conceptual model of Cornwall from source location $270° = South$, (a) 3D view without faults, (b) 3D view with faults, (c) 2D, top-down view, without faults and (d) 2D, top-down view, with faults. The colour bar represents the amplitude of displacement of the wave.

3.3. Anisotropy

Fig. 9(a),(c),(e),(g) shows the azimuth-dependent Rayleigh wave velocities for the Los Humeros model for the four different arrays. The strike of the fault is indicated by a solid vertical line at an azimuth of 90° (270°; plots are symmetric around 180° and here and in the following, values in parentheses denote the equivalent azimuth +180°).

Overall, the anisotropy for the conceptual model of Los Humeros depicts a 4θ anisotropy response for all arrays, except for the random array which depicts 2θ anisotropy) (Fig. 9(c)). 4θ anisotropy, first demonstrated by Backus [68] using perturbation theory, refers to the general form of the azimuthal dependence of the phase velocity of horizontally propagating P wave, which is a homogeneous trigonometric polynomial of degree 4 in θ, where θ is the azimuth of the horizontal wave vector [53] and is related to 90° symmetry [69]. This was then related to the azimuthal dependence of Rayleigh wave phase velocity by accounting for Rayleigh's principle by Smith and Dahlen [53]. This is written as a Fourier series in θ with five anisotropy coefficient [53], shown in Eq. (1).

The fastest velocities are observed around 60° (240°) for all but the random array, deviating significantly (by up to 40°) from the fault strike; similarly for the secondary peak at around 125° (305°). For the random array, we observe a fast direction at $\simeq 80°$ close to the true fault strike and no pronounced secondary peak in the anisotropy curve.

The slowest velocities (troughs) occur around $0 - 20°$ ($180 - 200°$) for all arrays, that is, close to the direction perpendicular to the fault. Local minima in the curves derived from the circular and the GEMex array coincide with the direction parallel to the fault at 90° (270°).

The magnitude of anisotropy (a_{mag}), is defined as half the difference between fastest and slowest velocities as a percentage of the isotropic velocity [49], varies between around 2.4% measured with the rectangular array and 7.3% for the GEMex array (all anisotropy parameters can be seen Table A.3).

(a) Source from the South
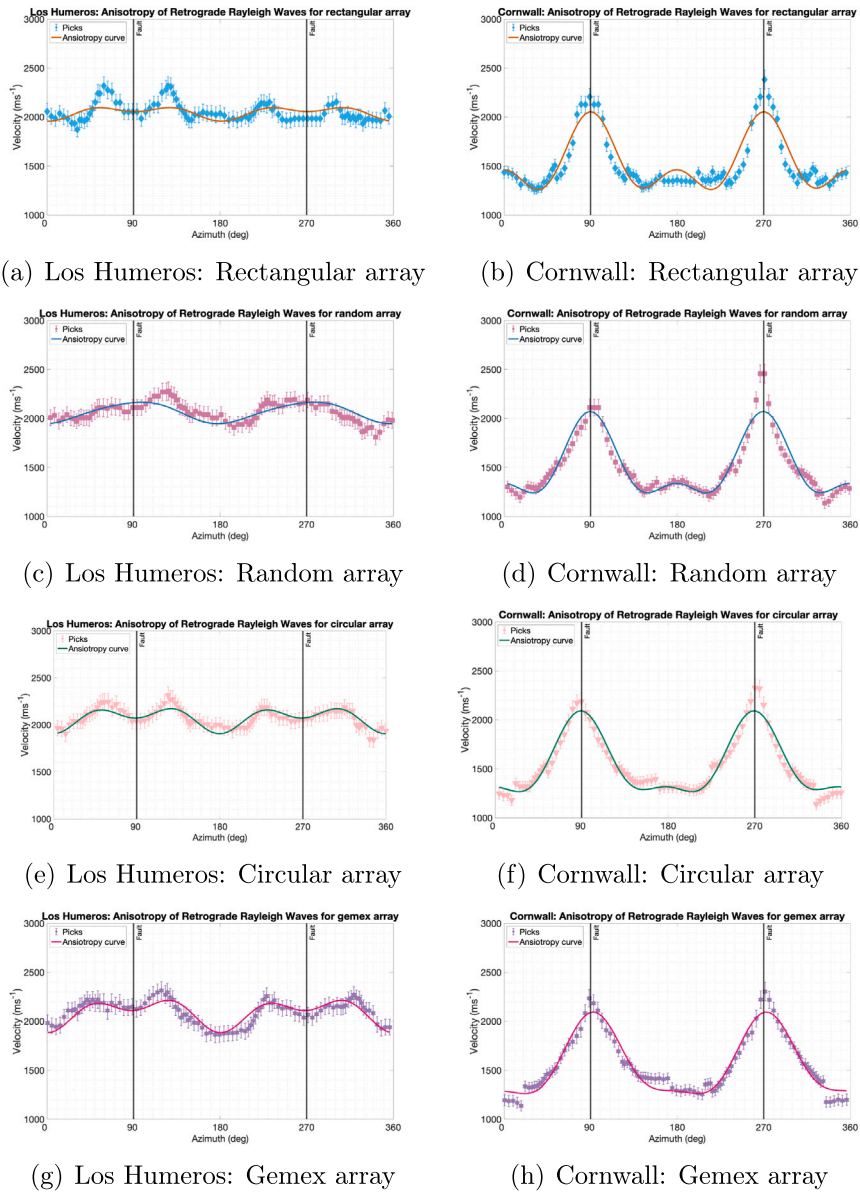

(b) Source from the East
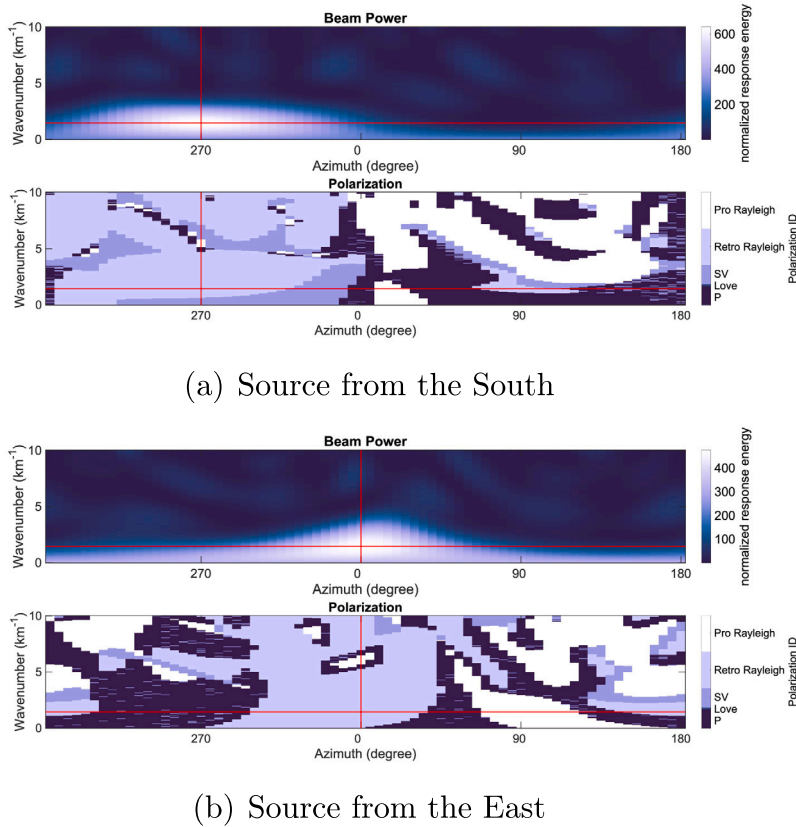
Fig. 8. Beampower plots for a conceptual model of Los Humeros with faults, from the GEMex array, for two different source locations, (a) time window = 13 (1.54 to 1.65 s), 270° = *South* on the *x*-axis and (b) time window = 13, 0° = *East* on the *x*-axis (East).

Fig. 9(b),(d),(f),(h) provides the azimuth-dependent Rayleigh wave velocities for the Cornwall model, granite with clay-filled faults. The periodic velocity pattern has large velocity variations, and cannot be described as a 4θ response (especially for the circular and gemex arrays, Fig. 9(f) and (h)). Fig. 9(b),(d),(f),(h) shows the fast directions (peaks) are parallel to the fault strike at azimuth 90° (270°) and the slow directions (troughs) are at azimuths 45° (225°) and 150° (330°).

The slowest velocities at azimuths of 330° and 150° are within a range of ±30° from 0° (or 360°) and 180° azimuth (perpendicular to faults), with increases to the maximum velocities at the parallel azimuths (90° and 270°) respectively. Differences in velocity depending on array design are minimal, with the random array providing overall slower velocities. Importantly, the fastest velocities for the Cornwall model are measured parallel to the faults. The magnitude of anisotropy (a_{mag}), which is the percentage of anisotropy variation between the smallest and largest anisotropic values [25], varies between around 21.3% measured with the random array and 28.3% for the circular array (all anisotropy parameters can be seen Table A.4).

Simulations for both scenarios for all azimuths were made on models without faults present (shown in Fig. 10). Fig. 10(a) shows the apparent anisotropy. These tests were done to assess the effect of the array design. Fig. 10(a) shows that the fastest velocities are at 130° and 360°, with the slowest velocities at 90°. The overall velocity range is small or smaller than the examples with faults, 400 ms^{-1}, and the fastest velocity (2450 ms^{-1}) is slightly faster than the expected isotropic velocity (around $V_R = 0.9 \times V_S$) at 2430 ms^{-1}.

Differences between anisotropy for different array designs also indicate a minimal array effect. Additionally, the peaks and troughs differ from those observed in the heterogeneous models for Los Humeros, confirming that these are indeed caused by the presence of a fault. Cornwall has a much smaller anisotropic response from the homogeneous simulations (Fig. 10(b)). In this example, there is a relatively constant velocity of 2300 ± 100 ms^{-1}, which is slower than the expected isotropic velocity of 2700 ms^{-1} but is inside the expected uncertainty range. Furthermore, the apparent anisotropy has minor velocity variations, with the largest differences being caused by rectangular arrays, showing that rectangular arrays are the least ideal for anisotropy analysis. However, the lack of difference in anisotropy pattern is noteworthy for the different array types, when more variation would be anticipated, this is discussed further in Section 4.1.

(a) Los Humeros: Rectangular array

(b) Cornwall: Rectangular array

(c) Los Humeros: Random array

(d) Cornwall: Random array

(e) Los Humeros: Circular array

(f) Cornwall: Circular array

(g) Los Humeros: Gemex array

(h) Cornwall: Gemex array

Fig. 9. Azimuth of source vs velocity picks with fitted anisotropy curves for Retrograde Rayleigh waves for Los Humeros (a),(c),(e),(f) a_{mag} range of 2.4 to 7.3% and Cornwall (b),(d),(f),(h) a_{mag} range of 21.3 to 28.3%, for (a) and (b) Rectangular array, (c) and (d) random array, (e) and (f) Circular array and (g) and (h) Gemex array. Azimuth steps are 2.3°, 270° is parallel to faults, and 0° is perpendicular to faults. Black lines depict the fault strike, and anisotropy curves are fitted to data picks using the to function of (a, θ) of Eq. (1) and sorted with a nonlinear programme solver that finds the local minimum of the fit, called fminunc (for details refer to Mathworks [70]). (For interpretation of the references to colour in this figure legend, the reader is referred to the web version of this article.)

3.3.1. Importance of source location

Throughout various ambient seismic studies [56,58,59], the receiver layout is always treated with a degree of care to obtain optimal results, whereas the source layout tends to be not considered to the same degree. However, the source layout is frequently analysed in interferometric approaches where isotropic noise sources are needed to calculate stable and unbiased Green's functions [50]. Often beamforming is used to estimate the homogeneity of the noise wavefield with respect to azimuths [50]. The anisotropy curves for the different source locations can be seen in Fig. 11.

Using a diamond shape instead of a circle, we deliberately vary the source-array distance with azimuth so that Rayleigh waves arrive at the array in different time windows for different sources. Fig. 11 shows that there is more anisotropy velocity variation for the diamond source layout than the relatively constant velocity for the circular source layout (with the exception of 35°).

(a) Model of Los Humeros (b) Model of Cornwall
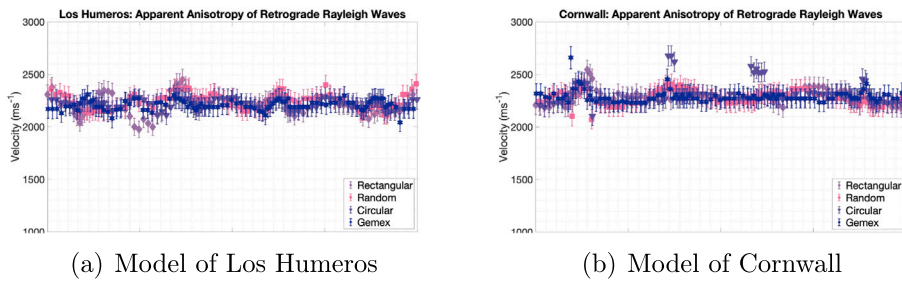
Fig. 10. Apparent anisotropy for Retrograde Rayleigh waves for all array designs, for (a) conceptual model of Los Humeros and (b) conceptual model of Cornwall. Azimuth steps are ≃ 2.3°.

(a) Model (b) Cornwall, GEMex array: Anisotropy curve
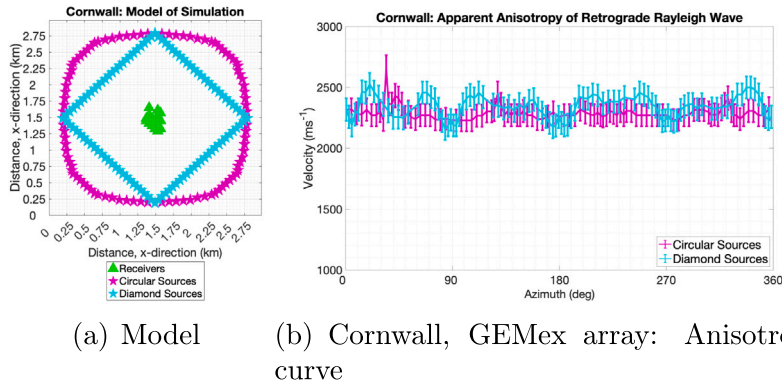
Fig. 11. Apparent anisotropy for Retrograde Rayleigh waves for the GEMex array design with the diamond vs circulars distribution for Cornwall without faults (a) Model of two different source layouts, for (b) Anisotropy curves for GEMex array with different source layouts. Azimuth steps are ≃ 2.3°.

4. Discussion

We used numerical modelling to generate Rayleigh waves in faulted models and performed anisotropy analysis on synthetic array data using three-component beamforming. The main observations are that the array design has only a minor impact on the observed anisotropy while the geology, such as the difference in V_S for the different scenarios, greatly impacts the anisotropy response.

4.1. True vs measured azimuth

The azimuth obtained from the beamformer could be slightly influenced by the faults and source azimuth. Fig. 9, Figs. 10 and 11(b) all refer to the velocity vs known azimuth of the various scenarios that they depict. The known azimuth is the azimuth calculated based on the known source location, instead of the measured azimuth as extracted from the beamformer. Fig. 12 shows the variation of velocity as a function of known and measured azimuth for a conceptual model of Los Humeros with faults using wavefield values from the GEMex array layout. Fig. 12 shows that B3AM extracts azimuths very closely to the known azimuth of the sources, with a deviation in the range of the azimuth grid resolution (5°). The largest degree of azimuth offset is in the fast directions, shifting both further from the strike of the fault at 270°. Even though the difference between known and measured azimuth is small, consideration must be taken when looking at the fast directions, accounting for potential offset of azimuth relative to fault strike when looking at fault strikes in real data.

4.2. Effects of acquisition geometry

Next, let us consider the array effects shown by the beamformer. To focus on the apparent anisotropy effect from different arrays and only arrays with a similar number of stations (17) but different layouts were considered, to not alter too many properties at the same time. Therefore, the 100-receiver array is not used to its full capacity and varying receiver numbers are beyond the scope of this study.

Referring back to Fig. 9 when comparing the multiple different arrays to each other the fast directions are relatively consistent for the Cornwall model, which is indicative of a small array effect. Comparatively, for Los Humeros the array effect is not negligible, with the random array providing the least consistent fast direction and the poorest fitting. This provides a perspective into the behaviour of the different arrays regarding anisotropy analysis. Moreover, between 345° and 15°, some retrograde Rayleigh waves

12

Fig. 12. Known Azimuth vs Measured Azimuth of source as a function of velocity for Retrograde Rayleigh waves for GEMex array, for a conceptual model of Los Humeros. 270° is parallel to faults, and 0° is perpendicular to faults (depicted by black lines). Error bars are 5% of the velocity. (For interpretation of the references to colour in this figure legend, the reader is referred to the web version of this article.)
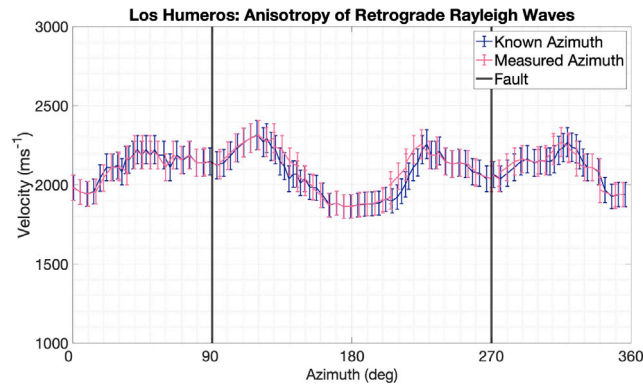

(a) Model of Los Humeros
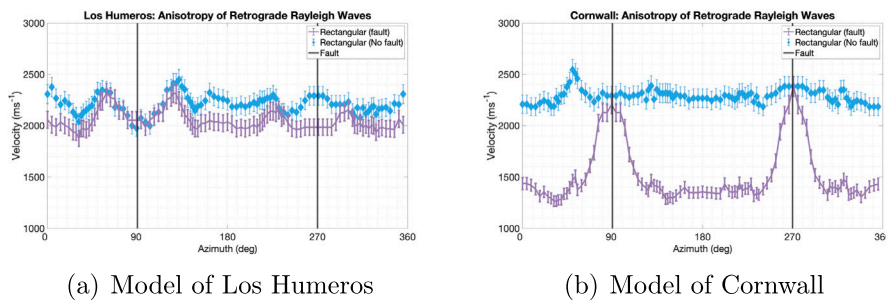
(b) Model of Cornwall

Fig. 13. Velocity vs azimuth for models with and without fault for the rectangular array, for (a) the model of Los Humeros and (b) for the model of Cornwall. Azimuth steps are $\simeq 2.3°$.

could not be identified within a given time window for some array layouts, indicating that velocities from different arrays that are drastically different must be scrutinised.

Fig. 10 provides a comparison of all array types for both models without faults present. This conveys the velocity variation pattern for the different arrays, with the rectangular array having the most dramatic differing velocity changes. For this case we look at an example of anisotropy without faults being present and compare it to previous results for the two fractured models as shown in Fig. 13.

For the rectangular array in the Los Humeros model, Fig. 13(a) shows the differences between the homogeneous (without fault) and heterogeneous (with fault) models. Parallel to the fault (90°) the velocities for both models are similar, which indicates a decrease in the observed velocities (with a fault) at this angle due to the array. Furthermore, at 60° and 125° and 230°, there would be an increase in the observed velocities with a fault due to the rectangular array. Perpendicular to the fault (180°), there is a slight decrease in velocity for the homogeneous model, which will decrease the observed velocity at this azimuth for the heterogeneous model slightly. This would impact the interpretation of the fault strike from this anisotropy pattern. The anisotropy of Los Humeros (Fig. 13(a)) with and without the fault has a lot of similarity, especially around 90°, thus indicating some impact of the array on the anisotropy for Los Humeros.

For the rectangular array for the Cornwall model, Fig. 13(b) has a larger difference between the homogeneous and heterogeneous models. Parallel and perpendicular to the fault, there is a relatively constant velocity for the homogeneous model, which would not cause a change in the observed anisotropy pattern for the heterogeneous model. At 55° there is an increase in velocity for the homogeneous model, which would cause an increase in observed velocity at this azimuth for the heterogeneous model; this could explain the slight peak in the heterogeneous curve.

Overall, the most interesting outcome is how similar the results are for the Cornwall model for the different arrays, whilst there is some variation for the Los Humeros model for the different arrays. This may differ for an ambient noise scenario where the wavefield can be a superposition of multiple waves rather than one wave at a time, therefore the array may have a larger effect on the anisotropy in an ambient noise scenario.

Fig. 11 shows the effect of source layout on Rayleigh wave velocity. Source-array distance affects the separation of wave types. The Rayleigh wave will have separated better from the P-wave when the distance is larger, while the overlap of P and Rayleigh will be more severe for shorter distances. This will influence how well the Rayleigh wave can be recognised by the beamformer and can lead to variations in the estimated velocities and, hence, bias the anisotropy analysis. We point out that this problem arises

Table 2
Parameters for all shear wave velocity difference conceptual models, showing the compressional velocity (V_p), shear velocity (V_s) and density (ρ) of both the surrounding rock, the "fill" of the fault and the damage zone of the fault. V_p and V_s in ms^{-1}, and ρ in kgm^{-3}. Values for velocity were chosen to maintain as constant a V_p/V_s as possible.

Velocity difference (ms^{-1})	Surrounding rock			Fault "fill"			Damage zone		
	V_p	V_s	ρ	V_p	V_s	ρ	V_p	V_s	ρ
1400	4800	3000	2640	2780	1600	1760	2880	1660	1660
1500	4800	3000	2640	2620	1500	1760	2720	1560	1660
1600	4800	3000	2640	2440	1400	1760	2540	1460	1660
1700	4800	3000	2640	2260	1300	1760	2360	1360	1660
2000	4800	3000	2640	1740	1000	1760	1840	1060	1660
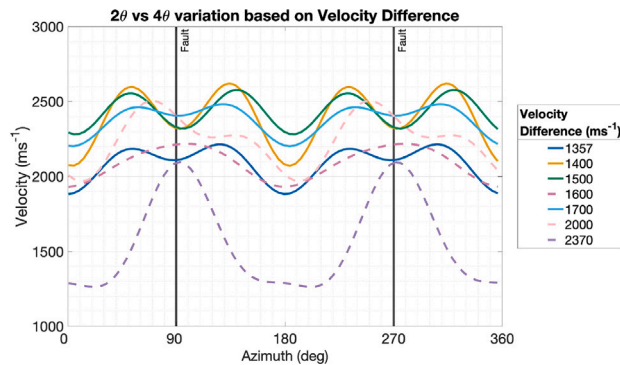
Fig. 14. Velocity vs azimuth for a range of velocity differences between the surrounding rock and the fault for GEMex array. Dashed lines depict 2 peaks in the anisotropy, and solid lines depict 4 peaks in the anisotropy, a_{mag} range of 5.9 to 11.7% (Table A.9) Fault strike represented by black lines. (For interpretation of the references to colour in this figure legend, the reader is referred to the web version of this article.)

only when considering transient waves from individual point sources, as in the numerical model, rather than continuous noise signals. Hence, when Rayleigh waves are extracted from ambient noise and multiple time windows treated statistically (cf. [4]), the effect of the source-array spacing should not play a role. However, when beamforming is to be applied to identify and characterise wave types in transient signals, time window length and overlap can have a significant effect, and results might become more stable when adjacent time windows are analysed jointly. More testing is required to further quantify the behaviour and formulate recommendations for three-component beam response processing and interpretation of transient signals. In real life, however, the source distribution cannot be controlled or known in advance in most ambient noise applications [57].

4.3. Effect of geological parameters

Investigating different geological scenarios, we find that in the case of the model for Los Humeros, there is a smaller velocity contrast between fault fill and surrounding rock (see Table 1), which seems to result in an anisotropy with a more complex pattern (4θ) but which is less pronounced in amplitude. However, for the stronger contrast shown by the model Cornwall, we observe either 2θ or 4θ anisotropy, depending on the array geometry, with an unambiguous fast direction. Fig. 9(b),(d),(f),(h) indicates that the Rayleigh waves travelling parallel to the fault are faster. If the V_S of the surrounding rock and fault-"fill" have a large difference between each other, the anisotropy curve will have higher amplitudes due to dramatic velocity changes.

We assess the point at which the relationship between the velocity of the surrounding rock and fault-"fill" causes a change from 2θ to 4θ anisotropy by testing additional models with varying velocity contrasts between rock and fault-"fill" (parameters are shown in Table 2). Fig. 14 shows how the anisotropy response changes from 4θ to 2θ when the difference in velocity for the surrounding rock and fault-"fill" increases (1357 ms^{-1} difference in the model for Los Humeros). When the velocity difference between the rock and the fault-"fill" is 1500 ms^{-1} or less, 4θ anisotropy is observed (expressed by two clear velocity peaks). The dominant slow direction occurs perpendicular to the fault in these cases. For the largest velocity contrast of 2370 ms^{-1} (Cornwall model) the anisotropy pattern again shows a 4θ periodicity, however, this time we observe two slow directions and one dominant fast direction aligning with the fault strike.

Further, a velocity difference of 2370 ms^{-1} provides the lowest mean velocity for the anisotropy curve, of $\simeq 1600$ ms^{-1} compared to the model with a velocity difference of 1400 ms^{-1} which provides the highest mean velocity of $\simeq 2400$ ms^{-1}. Why there is such a dramatic decrease in mean velocity for a velocity difference of 2370 ms^{-1} compared to the others leaves a question for a future study.

4.4. Observed versus structural anisotropy

The observed anisotropy and structural anisotropy for the model of Cornwall are the same (Fig. 9(b),(d),(f),(h)), with the fast directions at azimuths of 90° and 270°. The observed anisotropy for the model of Los Humeros (Fig. 9(a),(c),(e),(g)), has fast directions at 30° ± 20° on either side of the structural anisotropy (90° and 270°).

However, the slow directions may provide a better indication of the fault strike depending on the velocity contrast: For the Los Humeros morel, which has a small velocity contrast between the rock and the faults, the slowest direction for the observed anisotropy is perpendicular to the fault strike On the other hand, the model for Cornwall with its high velocity contrast has the fast directions parallel to the fault strike and a significantly lower velocity perpendicular to the fault. This indicates that, in general, the slow directions, as seen by the beamformer, may be more representative of the structural anisotropy of the subsurface than the fast direction depending on the velocity contrast of the fractured media.

4.5. Comparison to Los Humeros data

Numerical modelling can create a conceptual model to get a complex anisotropy response, similar to patterns seen in real data of fractured media. A previous study [71] underwent full waveform ambient noise inversion using numerical simulations to improve the inversion scheme for tomography. Chaput et al. [72] used numerical analysis to assess the depth sensitivity of Rayleigh waves due to their multi-modal behaviour. However, they found that the numerical models did not explain why the inferred fast directions aligned with the direction of ice flow at high frequencies.

Looking at the results for the GEMex array design for Fig. 9(g) for Los Humeros, to Fig. 3 there are similarities in anisotropic curves. However, the numerical results have higher amplitudes (larger velocity fluctuations) than the real data, with both numerical and real results exhibiting the 4θ anisotropy. The higher amplitudes can potentially be reduced by accounting for the apparent anisotropy, although some complexity will remain. This study shows that 4θ anisotropy can result from only one fault orientation (the five faults modelled having the same strike) that exhibits a relatively small velocity contrast with the surrounding rock. The main difference is that we do not assume a perfectly NS striking fault for Los Humeros in the real results, so we cannot compare the two plots directly. Numerical results indicate that the slow direction is linked to the fault strike within a fractured medium, indicating the direction perpendicular to the fault strike. Interpreting the data in Fig. 3 based on these findings, the slow direction of 90° (North) implies a 0° (East-West) striking fault, which corresponds to the strike of some of the known resurgence faults in Los Humeros [7,73].

Numerical models can never be a perfect replica of the real world, but they can provide some useful insights into the degree of complexity we can expect from real data and, therefore, the corresponding anisotropic structure. Furthermore, even relatively simple structures can cause 4θ anisotropy.

4.6. Future: More complex models

Faults vary with depth, and the maximum depth of penetration of the faults can be assessed by observing retrograde Rayleigh waves as a function of frequency. A depth-dependent numerical model would allow for the observation of this relationship with depth, which requires more computational resources than used in this study. Frequency-dependent analysis, could provide an insight into the variation of anisotropy of a model of fractured media at depth and, consequently, its comparability to real anisotropy data at depth.

5. Conclusions

This study has used numerical modelling to analyse synthetic Rayleigh waves in fractured media, revealing nonlinear anisotropic wave behaviour which is identified and characterised using three-component (3C) beamforming of the synthetic wavefield. A previous study [7] hypothesised that the fast direction of Rayleigh wave propagation aligns with the fault strike. However, numerical modelling indicates that this is not always the case. We find that the velocity contrast between fault and surrounding rock controls the complexity and magnitude of the observed anisotropy: a smaller contrast leads to smaller magnitudes but larger complexity/ambiguity (4θ anisotropy), whereas a larger contrast results in larger magnitudes and lower complexity (2θ anisotropy). In the first case, the fast direction could differ by up to 50° from the fault strike. However, slow velocities seem to be aligning with the direction perpendicular to the fault strike when the velocity contrast between rock and fault is small and might, therefore, be a more reliable indicator for fault orientation. In the latter case, the fast direction aligns perfectly with the fault. We further observe variations in the estimated anisotropy depending on the chosen array design. These differences are small when the velocity contrast between fault and surrounding rock is large, however, they become more pronounced for small velocity contrasts and could lead to misinterpretation of the fault strike direction. Future research could investigate the effect of more complex source wavefields to address the gap to ambient noise analysis, as well as consider more realistic geological models.

CRediT authorship contribution statement

Heather Kennedy: Writing – review & editing, Writing – original draft, Methodology, Investigation, Formal analysis, Data curation, Conceptualization. **Claudia Finger:** Writing – review & editing, Supervision, Software, Resources, Formal analysis. **Katrin Löer:** Writing – review & editing, Supervision, Project administration, Formal analysis, Conceptualization. **Amy Gilligan:** Writing – review & editing, Supervision, Formal analysis.

Declaration of competing interest

The contact author declares that none of the authors have conflicts of interest.

Appendix A. Supplementary results

See Figs. A.15 and A.16 and Tables A.3–A.9.

The magnitude of anisotropy (a_{mag}) was calculated using half the difference between the fastest and the slowest velocities as a percentage of the sum of the percentage of the isotropic velocity [25].

(a) Rectangular array

(b) Random array

(c) circular array
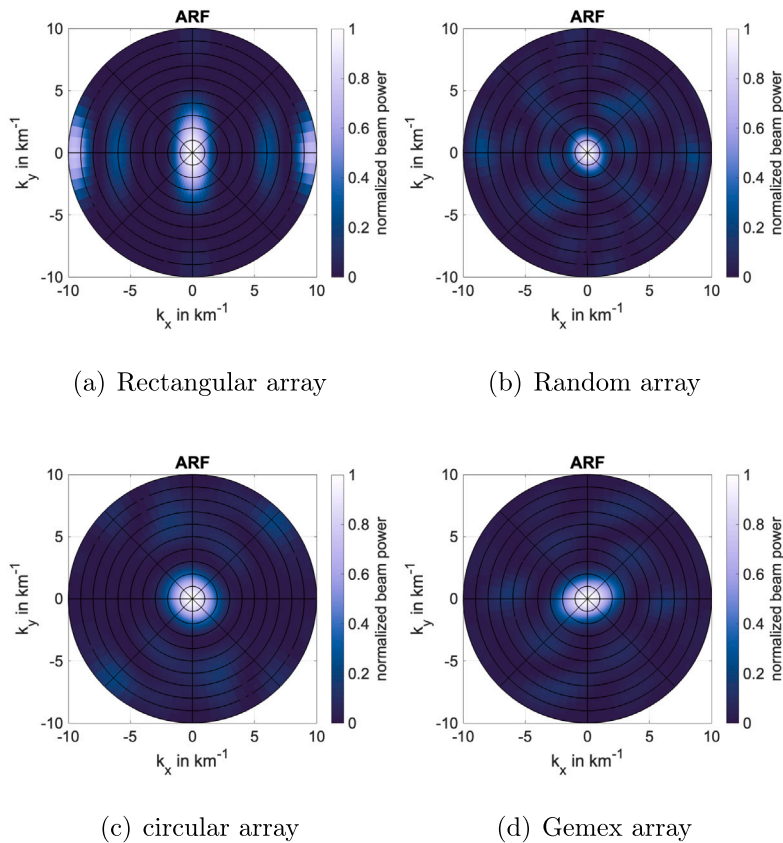
(d) Gemex array

Fig. A.15. Theoretical array responses for (a) rectangular array, (b) random array, (c) circular array and (d) gemex array.

Table A.3

Anisotropy parameters and magnitude of anisotropy (a_{mag}) for the different array designs for the model of Los Humeros, Fig. 9(a), (c), (e), (g).

Array	a_{mag} (%)	a_0	a_1	a_2	a_3	a_4
Rectangular	2.473	2.048	−0.049	−0.003	−0.0411	−0.004
Random	4.668	2.064	−0.107	−0.005	−0.010	0.009
Circular	5.798	2.072	−0.084	−0.004	−0.083	0.004
GEMex	7.386	2.090	−0.113	−0.013	−0.093	0.003

(a) Rectangular array

(b) Random array

(c) circular array

(d) Gemex array
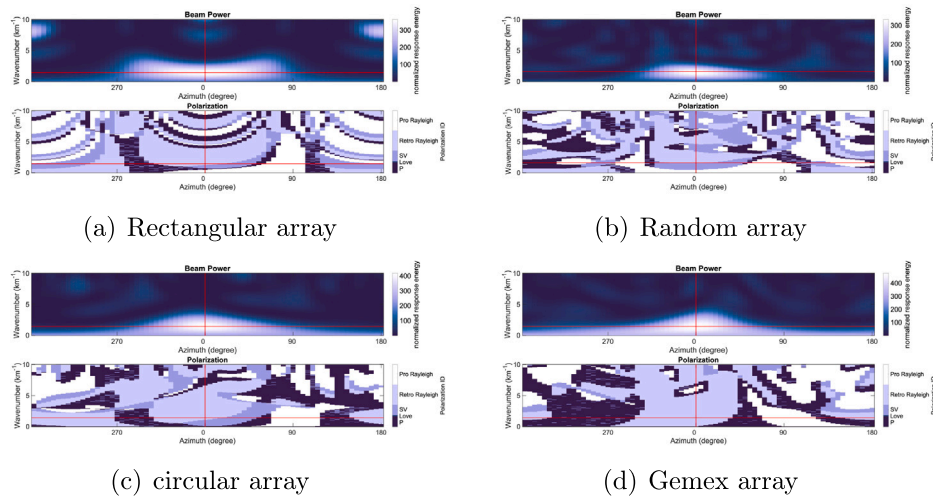
Fig. A.16. Beampower plots for three different array designs (17 receivers, 16 for rectangular) for Los Humeros with faults, for the source at $0° = East$ for area (1) without faults. (a) time window = 13 (1.53 to 1.65 s), rectangular array, (b) time window = 8, random array, (c) time window = 13, circular array and (d) time window = 13, gemex array. Each plot shows a Retrograde Rayleigh wave as the identifiable wave type in their respective time window's, note that it is normal for the identifiable desired wave type to be within ± 2.

Table A.4

Anisotropy parameters and magnitude of anisotropy (a_{mag}) for the different array designs for the model of Cornwall, Fig. 9(b), (d), (f), (h).

Array	a_{mag} (%)	a_0	a_1	a_2	a_3	a_4
Rectangular	23.004	1.538	−0.296	−0.0072	0.221	−0.001
Random	21.287	1.518	−0.367	0.005	0.187	−0.006
Circular	28.349	1.553	−0.388	0.002	0.152	−0.012
GEMex	23.096	1.570	−0.402	−0.054	0.119	0.0144

Table A.5

Anisotropy parameters and magnitude of anisotropy (a_{mag}) for the GEMex array for the different velocity variations.

Velocity difference (ms^{-1})	a_{mag} (%)	a_0	a_1	a_2	a_3	a_4
1400	11.701	2.397	−0.121	−0.0256	−0.197	−0.047
1500	5.902	2.433	−0.016	−0.015	−0.121	−0.054
1600	6.831	2.090	−0.141	−0.011	−0.017	0.008
1700	5.962	2.380	−0.010	−0.0217	−0.0738	−0.017
2000	10.216	2.280	−0.059	0.006	0.060	−0.010

Table A.6

Array coordinates for the Rectangular array, values are in grid points (one grid point is 10 m) for the z, x and y-direction.

z-direction	x-direction	y-direction
5	134	142
5	134	146
5	134	150
5	134	154
5	146	142
5	146	146
5	146	150
5	146	154
5	154	142
5	154	146
5	154	150
5	154	154
5	166	142
5	166	146
5	166	150
5	166	154

Table A.7
Array coordinates for the Random array, values are in grid points (one grid point is 10 m) for the z, x and y-direction.

z-direction	x-direction	y-direction
5	166	134
5	158	162
5	166	146
5	154	142
5	130	142
5	162	130
5	162	158
5	166	154
5	154	166
5	154	158
5	142	150
5	150	162
5	134	150
5	154	134
5	130	138
5	138	142
5	166	150

Table A.8
Array coordinates for the Circular array, values are in grid points (one grid point is 10 m) for the z, x and y-direction.

z-direction	x-direction	y-direction
5	134	150
5	138	142
5	142	158
5	142	138
5	146	142
5	146	154
5	150	134
5	150	146
5	150	162
5	150	158
5	154	142
5	154	158
5	158	154
5	158	158
5	158	142
5	162	146
5	166	150

Table A.9
Array coordinates for the Gemex array, values are in grid points (one grid point is 10 m) for the z, x and y-direction.

z-direction	x-direction	y-direction
5	138	146
5	142	142
5	146	138
5	150	134
5	154	130
5	158	134
5	154	138
5	158	146
5	150	146
5	146	150
5	142	150
5	138	150
5	142	154
5	142	166
5	154	162
5	158	158
5	154	154

A.1. Array coordinates

The array coordinate values are listed in the tables below, each table for each array. It is worth noting that the values are in grid points (as specified by the numerical model), not in typical coordinate units.

Data availability

Data will be made available on request.

References

[1] N.A. Haskell, The dispersion of surface waves on multilayered media, Vincit Verit.: A Portrait the Life Work. Norman Abraham Haskell, 1905– 1970 30 (1990) 86–103.

[2] P.D. Bromirski, F.K. Duennebier, The near-coastal microseism spectrum: Spatial and temporal wave climate relationships, J. Geophys. Res.: Solid Earth 107 (B8) (2002) ESE–5.

[3] S. Rost, C. Thomas, Array seismology: Methods and applications, Rev. G Eophysics 40 (3) (2002) 1–2.

[4] N. Riahi, G. Bokelmann, P. Sala, E.H. Saenger, Time-lapse analysis of ambient surface wave anisotropy: A three-component array study above an underground gas storage, J. Geophys. Res.: Solid Earth 118 (10) (2013) 5339–5351.

[5] K. Tokimatsu, S. Tamura, H. Kojima, Effects of multiple modes on Rayleigh wave dispersion characteristics, J. Geotech. Eng. 118 (10) (1992) 1529–1543.

[6] N. Wang, J.-P. Montagner, G. Burgos, Y. Capdeville, D. Yu, Intrinsic versus extrinsic seismic anisotropy: Surface wave phase velocity inversion, Comptes R Endus. GÉoscience 347 (2) (2015) 66–76.

[7] H. Kennedy, K. Löer, A. Gilligan, Constraints on fracture distribution in the Los Humeros geothermal field from beamforming of ambient seismic noise, Solid Earth 13 (12) (2022) 1843–1858.

[8] S. Luo, H. Yao, Multistage tectonic evolution of the Tanlu fault: Insights from upper crustal azimuthal anisotropy of the Chao Lake segment, Tectonophysics 806 (2021) 228795.

[9] Z. Li, Z. Peng, Stress-and structure-induced anisotropy in southern California from two decades of shear wave splitting measurements, Geophys. R Esearch L Etters 44 (19) (2017) 9607–9614.

[10] N.L. Boness, M.D. Zoback, Mapping stress and structurally controlled crustal shear velocity anisotropy in California, Geology 34 (10) (2006) 825–828.

[11] J.F. Bauer, M. Krumbholz, S. Meier, D.C. Tanner, Predictability of properties of a fractured geothermal reservoir: the opportunities and limitations of an outcrop analogue study, Geotherm. Energy 5 (1) (2017) 1–27.

[12] Z. Liu, J. Huang, H. Yao, Anisotropic Rayleigh wave tomography of Northeast China using ambient seismic noise, Phys. the E Arth P Lanetary I Nteriors 256 (2016) 37–48.

[13] A. Li, D.W. Forsyth, K.M. Fischer, Shear velocity structure and azimuthal anisotropy beneath eastern North America from Rayleigh wave inversion, J. G Eophysical R Esearch: S Olid E Arth 108 (B8) (2003).

[14] C.P. Legendre, L. Zhao, W.-G. Huang, B.-S. Huang, Anisotropic Rayleigh-wave phase velocities beneath northern Vietnam, Earth, P Lanets S Pace 67 (2015) 1–16.

[15] S. Crampin, Shear-wave splitting: new geophysics and earthquake stress-forecasting, Encycl. Solid Earth Geophys. (2020) 1–11.

[16] H.-W. Shan, B. Tian, C.-D. Cheng, X.-T. Gao, Y.-Q. Chen, H.-D. Liu, N-soliton and other analytic solutions for a (3+ 1)-dimensional Korteweg–de Vries–Calogero–Bogoyavlenskii–Schiff equation with the time-dependent coefficients for the shallow water waves, Qual. T Heory D Ynamical S Ystems 23 (Suppl 1) (2024) 267.

[17] C.-H. Feng, B. Tian, X.-T. Gao, Bilinear form, N solitons, breathers and periodic waves for a (3+ 1)-dimensional Korteweg-de Vries equation with the time-dependent coefficients in a fluid, Qual. T Heory D Ynamical S Ystems 23 (1) (2024) 291.

[18] X.-Y. Gao, In an ocean or a river: bilinear auto-bäcklund transformations and similarity reductions on an extended time-dependent (3+ 1)-dimensional shallow water wave equation, China O Cean E Ngineering 39 (1) (2025) 160–165.

[19] R.T. Lacoss, E.J. Kelly, M.N. Toksöz, Estimation of seismic noise structure using arrays, Geophysics 34 (1) (1969) 21–38.

[20] J. Capon, High-resolution frequency-wavenumber spectrum analysis, Proc. IEEE 57 (8) (1969) 1408–1418.

[21] C. Esmersoy, V. Cormier, M. Toksöz, Three-component array processing, the VELA program: A twenty-five year review of basic research a, AV Kerr (1985) 565–578.

[22] R. Schmidt, Multiple emitter location and signal parameter estimation, IEEE Trans. Antennas and Propagation 34 (3) (1986) 276–280.

[23] J. Benesty, J. Chen, Y. Huang, Conventional beamforming techniques, Microphone Array Signal Process. (2008) 39–65.

[24] K. Löer, B3AM: MATLAB toolbox for three-component beamforming (1.0), 2024, Retrieved March 27, 2024, Zenodo. Available at DOI:10.5281/zenodo.10885984.

[25] K. Löer, N. Riahi, E.H. Saenger, Three-component ambient noise beamforming in the Parkfield area, Geophys. J. Int. 213 (3) (2018) 1478–1491.

[26] E.H. Saenger, N. Gold, S.A. Shapiro, Modeling the propagation of elastic waves using a modified finite-difference grid, Wave Motion 31 (1) (2000) 77–92.

[27] T. Bohlen, E.H. Saenger, Accuracy of heterogeneous staggered-grid finite-difference modeling of Rayleigh waves, Geophysics 71 (4) (2006) T109–T115.

[28] L.M. Weydt, K. Bär, I. Sass, Petrophysical characterization of the Los Humeros geothermal field (Mexico): from outcrop to parametrization of a 3D geological model, Geotherm. Energy 10 (1) (2022) 5.

[29] K.E. Schulz, K. Bär, I. Sass, Lab-scale permeability enhancement by chemical treatment in fractured granite (Cornubian batholith) for the united downs deep geothermal power project, cornwall (UK), Geosciences 12 (1) (2022) 35.

[30] M. Takarli, W. Prince, Permeability and P-wave velocity change in granitic rocks under freeze–thaw cycles, Geomech. Geoengin.: An Int. J. 2 (3) (2007) 227–234.

[31] R. Scrivener, D. Highley, D. Cameron, K. Linley, R. White, Mineral resource information for development plans phase one cornwall: Resources and constraints, 1997.

[32] M.A. Kassab, A. Weller, Study on P-wave and S-wave velocity in dry and wet sandstones of tushka region, Egypt, Egypt. J. Pet. 24 (1) (2015) 1–11.

[33] GPG, Seismic velocities of rocks and various materials, 2024, Available at https://gpg.geosci.xyz/content/physical_properties/tables/seismic_velocity.html,

[34] Y. Wang, Frequencies of the ricker wavelet, Geophysics 80 (2) (2015) A31–A37.

[35] M. Lowe, Wave propagation | guided waves in structures, in: S. Braun (Ed.), Encyclopedia of Vibration, Elsevier, Oxford, 2001, pp. 1551–1559, http://dx.doi.org/10.1006/rwvb.2001.0173, Available at https://www.sciencedirect.com/science/article/pii/B0122270851001739.

[36] E.G. Limited, Eden geothermal – unlocking the energy from the rocks beneath our feet, 2024, Available at https://www.edengeothermal.com/.

[37] L. Ferrari, T. Orozco-Esquivel, V. Manea, M. Manea, The dynamic history of the trans-mexican volcanic belt and the Mexico subduction zone, Tectonophysics 522 (2012) 122–149.

[38] E. Jolie, D. Bruhn, A.L. Hernández, D. Liotta, V.H. Garduño-Monroy, M. Lelli, G.P. Hersir, C. Arango-Galván, D. Bonté, P. Calcagno, P. Deb, C. Clauser, A.F.H. Peters, E. Huenges, Z.I.G. Acevedo, K. Kieling, E. Trumpy, J. Vargas, L.C. Gutiérrez-Negrín, A. Aragón-Aguilar, S. Halldórsdóttir, E.G. Partida, GEMex - A Mexican-European Research cooperation on development of superhot and engineered geothermal systems - Proceedings, Stanford, CA, USA, 2018.

[39] G. Norini, G. Groppelli, R. Sulpizio, G. Carrasco-Núñez, P. Dávila-Harris, C. Pellicioli, F. Zucca, R. De Franco, Structural analysis and thermal remote sensing of the los humeros volcanic complex: Implications for volcano structure and geothermal exploration, J. Volcanol. Geotherm. Res. 301 (2015) 221–237.

[40] E. Fuentes-Guzmán, E. González-Partida, A. Camprubí, G. Hernández-Avilés, J. Gabites, A. Iriondo, G. Ruggieri, M. López-Martínez, The miocene tatatila-las minas IOCG skarn deposits (veracruz) as a result of adakitic magmatism in the trans-mexican volcanic belt, Bolet´ i N de la S Ociedad G Eológica M Exicana 72 (3) (2020).

[41] M.H.P. Bott, A. Day, D. Masson-Smith, The geological interpretation of gravity and magnetic surveys in devon and cornwall, Philos. Trans. R. Soc. Lond. Ser. A, Math. Phys. Sci. 251 (992) (1958) 161–191.

[42] D. Beamish, J. Busby, The cornubian geothermal province: heat production and flow in SW England: estimates from boreholes and airborne gamma-ray measurements, Geotherm. Energy 4 (2016) 1–25.

[43] C.C. Hawley, Geology and Beryllium Deposits of the Lake George (or Badger Flats) Beryllium Area, Park and Jefferson Counties, Colorado, United States Department of the Interior. United States Government Publishing Office, A23, 1969.

[44] D. Manning, C. Exley, The origins of late-stage rocks in the st austell granite—a re-interpretation, J. Geol. Soc. 141 (3) (1984) 581–591.

[45] S. Camm, The Geology and Landscape of Cornwall and the Isles of Scilly, Alison Hodge Publishers, 2011.

[46] B.W. Chappell, R. Hine, The Cornubian Batholith: an example of magmatic fractionation on a crustal scale, Resour. Geol. 56 (3) (2006) 203–244.

[47] J. Capon, R.J. Greenfield, R.J. Kolker, Multidimensional maximum-likelihood processing of a large aperture seismic array, Proc. the I E E E 55 (2) (1967) 192–211.

[48] M. Gal, A.M. Reading, N. Nakata, L. Gualtieri, A. Fichtner, Beamforming and polarization analysis, Seism. Ambient. Noise (2019) 32–72.

[49] K. Löer, T. Toledo, G. Norini, X. Zhang, A. Curtis, E.H. Saenger, Imaging the deep structures of los humeros geothermal field, Mexico, using three-component seismic noise beamforming, Seism. Soc. Am. 91 (6) (2020) 3269–3277.

[50] S. Schippkus, C. Hadziioannou, Matched field processing accounting for complex earth structure: method and review, Geophys. J Ournal I Nternational 231 (2) (2022) 1268–1282.

[51] P. Naghshin, H. Bahadori, Automatic extraction of retrograde and prograde Rayleigh waves from three-component earthquake signals in different depths of earth, Soil Dyn. Earthq. Eng. 147 (2021) 106800.

[52] S. Shaw, M.I. Othman, Characteristics of Rayleigh wave propagation in orthotropic magneto-thermoelastic half-space: An eigen function expansion method, Appl. Math. Model. 67 (2019) 605–620.

[53] M.L. Smith, F. Dahlen, The azimuthal dependence of Love and Rayleigh wave propagation in a slightly anisotropic medium, J. Geophys. Res. 78 (17) (1973) 3321–3333.

[54] Fminsearch MathWorks, 2024, (Accessed 05 January 2025), https://uk.mathworks.com/help/matlab/ref/fminsearch.html.

[55] J.C. Lagarias, J.A. Reeds, M.H. Wright, P.E. Wright, Convergence properties of the nelder–mead simplex method in low dimensions, S I A M J Ournal Optim. 9 (1) (1998) 112–147.

[56] J. Schweitzer, J. Fyen, S. Mykkeltveit, S.J. Gibbons, M. Pirli, D. Kühn, T. Kværna, Seismic arrays, in: New Manual of Seismological Observatory Practice 2 (NMSOP-2), Deutsches GeoForschungsZentrum GFZ, 2012, pp. 1–80.

[57] L. Lu, K. Wang, Z. Ding, The effect of uneven noise source and/or station distribution on the estimation of azimuth anisotropy of surface waves, Earthq. Sci. 31 (4) (2018) 175–186.

[58] S. Maranò, D. Fäh, Y.M. Lu, Sensor placement for the analysis of seismic surface waves: sources of error, design criterion and array design algorithms, Geophys. J. Int. 197 (3) (2014) 1566–1581.

[59] R.A. Haubrich, Array design, Bull. the Seism. Soc. Am. 58 (3) (1968) 977–991.

[60] S. Mykkeltveit, K. Åstebøl, D. Doornbos, E. Husebye, Seismic array configuration optimization, Bull. Seismol. Soc. Am. 73 (1) (1983) 173–186.

[61] A.K. Kerekes, Seismic array design by spatial convolution, Geophysics 66 (4) (2001) 1195–1207.

[62] K. Tokimatsu, J. Kōgakkai, I.S. of Soil Mechanics, E.G.E. Foundation Engineering. TC4, Geotechnical Site Characterization Using Surface Waves, 1995, Available at https://books.google.co.uk/books?id=eobAGwAACAAJ.

[63] M. Wathelet, D. Jongmans, M. Ohrnberger, S. Bonnefoy-Claudet, Array performances for ambient vibrations on a shallow structure and consequences over v s inversion, J. S Eismology 12 (2008) 1–19.

[64] J. Achenbach, Wave Propagation in Elastic Solids, Elsevier, 1973.

[65] X.-Y. Gao, Two-layer-liquid and lattice considerations through a (3+ 1)-dimensional generalized yu-toda-sasa-fukuyama system, Appl. M Athematics L Etters 152 (2024) 109018.

[66] X.-Y. Gao, Hetero-bäcklund transformation, bilinear forms and multi-solitons for a (2+ 1)-dimensional generalized modified dispersive water-wave system for the shallow water, Chin. J Ournal P Hysics 92 (2024) 1233–1239.

[67] X.-Y. Gao, Symbolic computation on a (2+ 1)-dimensional generalized nonlinear evolution system in fluid dynamics, plasma physics, nonlinear optics and quantum mechanics, Qual. T Heory D Ynamical S Ystems 23 (5) (2024) 202.

[68] G.E. Backus, Possible forms of seismic anisotropy of the uppermost mantle under oceans, J. Geophys. Res. 70 (14) (1965) 3429–3439.

[69] T. Ikeda, T. Tsuji, Azimuthal anisotropy of Rayleigh waves in the crust in southern Tohoku area, Japan, J. G Eophysical R Esearch: S Olid E Arth 119 (12) (2014) 8964–8975.

[70] Mathworks, Fminunc, 2024, (Accessed 07 February 2025), https://uk.mathworks.com/help/optim/ug/fminunc.html.

[71] K. Sager, L. Ermert, C. Boehm, A. Fichtner, Towards full waveform ambient noise inversion, Geophys. J Ournal I Nternational 212 (1) (2018) 566–590.

[72] J. Chaput, R. Aster, M. Karplus, N. Nakata, P. Gerstoft, P. Bromirski, A. Nyblade, R. Stephen, D. Wiens, Near-surface seismic anisotropy in antarctic glacial snow and ice revealed by high-frequency ambient noise, J. G Laciology 69 (276) (2023) 773–789.

[73] G. Norini, G. Carrasco-Núñez, F. Corbo-Camargo, J. Lermo, J.H. Rojas, C. Castro, M. Bonini, D. Montanari, G. Corti, G. Moratti, et al., The structural architecture of the los humeros volcanic complex and geothermal field, J. Volcanol. Geotherm. Res. 381 (2019) 312–329.